Chemical Physics Impact 12 (2026) 101060

Contents lists available at ScienceDirect

Chemical Physics Impact

journal homepage: www.sciencedirect.com/journal/chemical-physics-impact

Full Length Article

# High-density perovskite oxide ceramics with enhanced proton stopping power and gamma-ray shielding efficiency

Rahman I. Mahdi [a], K.A. Mahmoud [b,c], Nabil Janan Al-Bahnam [d], M.I. Sayyed [e,f], Kawa M. Kaky [g,h], Abed Jawad Kadhim [g,h], Yasser Maghrbi [i,j,*]

[a] Nanotechnology and Advanced Material Research Center, University of Technology-Iraq, Baghdad 10066, Iraq
[b] Nuclear Materials Authority, P.O. Box 530 El-Maadi, Cairo, Egypt
[c] Ural Federal University, 19 Mira St, 620002, Yekaterinburg, Russia
[d] Physics Department, College of Science for Women University of Baghdad, Baghdad, Iraq
[e] Department of Physics, Faculty of Science, Isra University, Amman, Jordan
[f] Department of Physics, Dogus University, Dudullu-Ümraniye, 34775, Istanbul, Türkiye
[g] Department of Medical Equipment Engineering, College of Engineering Technologies, Al-Nisour University, Baghdad, Iraq
[h] Department of Radiology and Sonography, College of Health & Medical Technologies, Al-Nisour University, Baghdad, Iraq
[i] Department of Mathematics and Natural Sciences, Gulf University for Science and Technology, Kuwait
[j] Université Côte d'Azur, Observatoire de la Côte d'Azur, CNRS, Laboratoire ARTEMIS, 06300 Nice, France

ARTICLE INFO

*Keywords:*
High-density compound
Titanium oxide
Nanomaterials
Gamma-ray shielding

ABSTRACT

In response to the growing demand for environmentally friendly radiation shielding materials, perovskite oxide ceramics emerge as a significant alternative to conventional radiation shielding solutions. This study investigated the radiation shielding properties of five high-density, different perovskite oxide ceramics ($BaTiO_3$ (BTO), $SrTiO_3$ (STO), $Bi_{0.5}Na_{0.5}TiO_3$ (BNT), $Bi_{0.5}K_{0.5}TiO_3$ (BKT), and $Bi_{0.5}Li_{0.5}TiO_3$ (BLT)). The X-ray confirms the successful formation of the perovskite structure of each one. Furthermore, the microstructure analysis shows a uniform particle morphology with an average particle size range from 95 to 780 nm. Stopping cross-section (SCS) and projected range have been evaluated for proton energy extending from 100 keV to 100 MeV. The ceramics trends' SCS has the order of SCS ($BaTiO_3$)> SCS ($SrTiO_3$)> SCS ($Bi_{0.5}K_{0.5}TiO_3$)> SCS ($Bi_{0.5}Na_{0.5}TiO_3$)> SCS (($Bi_{0.5}Li_{0.5}$)$TiO_3$) around the proton Bragg peak. Additionally, the γ-ray shielding efficacy of the synthesized ceramics was examined utilizing Monte Carlo simulation across the 0.015–15 MeV γ-ray energy range. The studies show that the $Bi_{0.5}K_{0.5}TiO_3$ composite's linear attenuation coefficient (LAC) exhibits the highest value, decreasing from 459.116 to 0.278 $cm^{-1}$ with a 0.015 MeV to 15 MeV γ-ray energy increase. This higher linear attenuation coefficient for $Bi_{0.5}K_{0.5}TiO_3$ lowers its lead-equivalent thickness and half-value thickness while it increases its radiation protection efficiency.

## 1. Introduction

Radiation shielding materials are essential in medical diagnostics, nuclear power systems, aerospace electronics, and nondestructive testing. Lead (Pb) and Pb-rich silicate or borate glasses have been a common shielding material for several decades due to Pb's high atomic number and density of around 11.3 g $cm^{-3}$, which makes it highly effective at blocking radiation. Lead is now known to be a widely toxic substance with no safe level of exposure, which has led to worldwide limits on its use and disposal [1]. The high demand for shields that are friendly to the environment with high performance has led to the creation of Pb-free heavy metal oxide glasses, polymers, composites, glass ceramics, concretes, and, more recently, high-density oxide ceramics [2–4].

$Bi_2O_3$ and BaO-rich borate or silicate matrix materials can achieve densities between 5 and 6 g $cm^{-3}$ and can match commercial lead glass in half value layer (HVL) performance. For example, Kaewkhao et al. showed that a 50 mol % $Bi_2O_3$–BaO borate glass attenuated 662 keV γ-rays more effectively than an equivalent PbO glass [5]. Glass suffers from several severe drawbacks, including brittleness and low thermal stability; high PbO or $Bi_2O_3$ content may lower viscosity and decrease temperature making it unsuitable for applications that require high

* Corresponding author.
*E-mail address:* Yasser.Maghrbi@univ-cotedazur.fr (Y. Maghrbi).

https://doi.org/10.1016/j.chphi.2026.101060
Received 15 February 2026; Received in revised form 8 April 2026; Accepted 15 April 2026
Available online 16 April 2026

loads or high-high heat environments. On the other hand, crystalline ceramics can be made to be harder, tougher, and more stable at high temperatures while still having the same densities by adding heavy cations.

The high electrical, optical, and mechanical properties, along with the thermal stability at high density, have attracted considerable attention to perovskite oxide ceramics [6–10]. For example, fully dense barium titanate $BaTiO_3$ sintered bodies have Vickers hardness a value of around 12 GPa and Young's modulus values of about 140 GPa, which are significantly higher than those of Pb-borate glasses with value of about 5 GPa [11–13]. Strontium titanate $SrTiO_3$ provides similar stiffness with slightly lower density. On the other hand, bismuth-based titanates like $Bi_{0.5}Na_{0.5}TiO_3$, $Bi_{0.5}K_{0.5}TiO_3$, and $Bi_{0.5}Li_{0.5}TiO_3$ have a high mass density ranging between 6.25 and 7.01 g $cm^{-3}$ and an atomic number structure that is similar to Pb. The result makes the photoelectric cross section in the 15 keV to 2 MeV range as high as possible [14–17]. In addition to being highly durable, these perovskites have multifunctional properties, such as electrochemical properties that are lacking in conventional lead glass. For example, $BaTiO_3$ is a high dielectric constant capacitor material, and $Bi_{0.5}Na_{0.5}TiO_3$-based and $Bi_{0.5}K_{0.5}TiO_3$-based solid solutions have strong piezoelectric coefficients and Curie temperatures above 280 °C. Their versatility means that they can be used to make shields that block radiation while also sensing or harvesting energy [18–21].

Replacing the harmful Pb with more environmentally friendly elements can offer significant benefits for both health and the environment. The manufacture and recycling of lead glass generate hazardous PbO dust; used shields must be treated as toxic waste. Substituting Pb with relatively friendly metals such as Bi, Ba, and Sr eliminates this risk. Dense Ba- and Bi-based ceramics are expected to provide comparable improvements in occupational safety, combined with enhanced mechanical strength and higher operation temperature.

Despite these advances, systematic comparisons of lead-free ceramics against conventional lead glasses over a truly broad γ-energy spectrum remain lacking. Most experimental studies still focus on the sub-MeV range or a single composition. For example, Boodaghi Malidarre et al. examined $(K_{0.5}Na_{0.5})NbO_3$-based relaxor ceramics only between 0.001 and 0.10 MeV [22], while Bendary et al. evaluated $Dy_2O_3$-modified sodium-boro-aluminate glass from 0.284 to 1.33 MeV [23]. Reactors and high-energy industrial sources operate above 1.3 MeV, where data primarily consists of isolated numerical estimates, leaving the 1.5–2.0 MeV window unexplored.

A recent systematic review on lead-free shielding materials showed that <15% of the 225 investigated studies used any mechanical or microstructural parameters when combined with attenuation data [24]. This splitting up of datasets keeps innovators from gaining the knowledge gap that they need, which includes integrated, composition-dependent property maps that cover energies from the diagnostic range of 60–140 keV to the reactor-relevant range of about 2 MeV and include both structural and functional properties. Filling this gap is therefore necessary for the rational substitution of toxic Pb-rich glasses with high-density, lead-free ceramics in next-generation radiation shielding systems. It's worth investigating oxide perovskites considering the $ABO_3$ lattice is very flexible. It allows for a number of modifications to its composition and significant defects while still keeping a recognizable perovskite structure. Such flexibility may also present some additional challenges. In Bi and alkali titanate perovskites, phase stability and consistency can be greatly affected by volatility, small stoichiometry shifts, oxygen vacancies, and secondary phases. Bismuth-based systems also show complex temperature and field driven structural behavior so linking composition, microstructure, and performance remains an active scientific topic.

The novelty of the current work is to fabricate and evaluate five dense lead-free ceramics to be applied for radiation shielding purposes. These ceramics were chosen to cover a representative perovskite compositional space spanning medium to high-Z cations. All ceramic compositions that were investigated in this study have the same $ABO_3$ perovskite structure that is built from corner sharing $TiO_6$ octahedra with different A-site cations. $BaTiO_3$ and $SrTiO_3$ ceramics are the well known alkaline earth titanate perovskites. BNT, BKT, and BLT ceramics are all solid solutions of the form $Bi_{0.5}A_{0.5}TiO_3$ where A is Na, K, or Li. They maintain charge balance on the A-site while varying ionic size and local distortion. These structures can show different symmetries even though the formulas are the same. This is consistent with the typical perovskite crystal chemistry and the tolerance factor concept which has long been used successfully for oxide perovskites and their distortions. We selected these specific perovskite oxides because they share the same structure type, but span clear and meaningful differences in A-site chemistry and density related parameters. This makes the comparison reasonable and helps connect patterns of shielding to composition while keeping the basic structure the same. X-ray diffraction verified the phase purity and crystalline structure, followed by microstructural examination by scanning electron microscopy to correlate density and grain morphology with shielding parameters.

The Stopping and Range of Ions in Matter (SRIM) code were used to calculate the electronic stopping cross-section (SCS) and projected range (PR) for proton movement in perovskite ceramics. Essential key parameters, including molar mass and the atomic number to atomic mass ratio (Z/A), for perovskite ceramics have been examined. Additionally, to investigate the fabricated composites' γ-ray shielding performance, the non-destructive Monte Carlo simulation tool was utilized. The effect of substituting Sr, Ba, Bi, Na, K, and Li ions on the shielding performance of the prepared perovskite structures was investigated.

## 2. Materials and methods

### 2.1. Preparation of samples

$BaTiO_3$, $SrTiO_3$, $Bi_{0.5}Na_{0.5}TiO_3$, $Bi_{0.5}K_{0.5}TiO_3$, and $Bi_{0.5}Li_{0.5}TiO_3$ were prepared by solid state reaction route. $BaCO_3$, CAS No. 513–77–9, purity 99.9%, $TiO_2$, CAS No. 13,463-67–7, purity 99.99%, $SrCO_3$, CAS No. 1633–05–2, purity 99.9%, $Na_2CO_3$, CAS No. 497–19–8, purity 99.9%, $Bi_2O_3$, CAS No. 1304–76–3, purity 99.99%, and $Li_2CO_3$, CAS No. 554–13–2, purity 99.9%, purchased from Sigma Aldrich, were used as the starting raw materials. The powders were first dried at 200 °C for 2 h to remove the moisture, especially for carbonate based raw materials. The materials were then weighed precisely, according to stoichiometric ratios corresponding to each ceramic. To obtain fine and mixed raw materials that probably enhance the chemical reaction, the ball milling process for 5 h using an ethanol medium was conducted. All five perovskite ceramics were prepared by a conventional solid state reaction; the raw materials were then placed in an alumina crucible covered with a lid and moved to a muffle furnace at 950 °C for 5 h in air, using a 2 °C/min heating ramp. These conditions were chosen because the synthesis of perovskites by solid state method typically need high temperature to complete diffusion and suppress secondary phases, and the literature shows that temperatures around ~950 °C are commonly used to obtain phase pure titanate perovskites [9,25,26]. In addition, we performed temperature trials and found that 950 °C for 5 h in air, at a ramping rate of 2 °C/min, gave the cleanest phase formation for our powders.

The crystalline structure of the materials was identified in a 2θ range from 10 to 70 using an X-ray diffraction (XRD) spectrometer, PANalytical Empyrean, Netherlands. The microstructure of the ceramics was examined with field emission scanning electron microscope (FE-SEM) Hitachi SU7000, Japan , and Tescan Mira 4, Czech Republic.

### 2.2. The Monte Carlo simulation for the γ-ray shielding properties

The Monte Carlo simulation (MCNP-5) evaluates the radiation shielding efficacy of synthesized ceramic composites from 0.015 to 15 MeV gamma photon energy range ($E_\gamma$). To complete the simulation, the

nuclear ENDF/B-VI.8 database should be integrated with MCNP-5 code to estimate the likelihood of gamma rays' interaction-cross section (σ) for each element constituting the synthesized ceramic composites. The input file for the MCNP-5 code must include a full description for a geometry consists of outer shielding cover, radioactive source, first collimators, synthesized lead-free ceramics, second collimator, and gamma-ray detector. These mentioned parts of the geometry introduced to the input file through many definite cards named cell, surface, mode, importance, radioactive source definition (SDEF), material, physical, cut-off, and tally cards [27].

A unit cell delineates each part in the geometry, where the number, density, material type, and importance of each cell was listed under the input file's cell cards. For each created cell, multiple surfaces must create to distinguish it from the surrounding environment. Dimensions of these created surfaces like radius, length, width, and thickness were all listed under the input files' surface card. The importance card is setup to be 1 for important cell in which the photon interaction is allowed, while it adjusted to be zero for unimportant cells in which the photon interaction isn't important. The mode card also was adjusted to be (mod: P) to allow the interaction of photons only. Furthermore, all information related to the radioactive sources used during the simulation process such as location (Pos 0 0 0), Energy (ENG: 0.015 - 15 MeV), emission direction (AXS: 0 0 1), particle type (PAR: 2 for photons), emission probability and the distribution of emitted particles all introduce to the input files SDEF card.

The outer Pb- shielding cylinder measures 25 cm in width, 5 cm in thickness, and 35 cm in height. The initial collimator was positioned between the γ-ray source and the prepared composites. The object possesses a radius of 3.5 cm, a height of 7 cm, and a vertical central slit of 0.5 cm to facilitate the perpendicular passage of photons through the engineered composites. The engineered nuclear shield composites and the detector system unit were separated by the secondary beam collimator, which possesses a radius (r) of 3.5 cm, a height of 3 cm, and a center vertical slit of 0.5 cm to allow γ-photons to traverse perpendicularly to the detector. After NPS of $10^8$ histories, the cutoff card was altered to finish a simulation and stop the interaction of photons with the electrons within the investigated ceramic samples. Subsequently, the output data file generated post-simulation presents the mean track length (MTL) of gamma photons within the cell containing the fabricated ceramics. The relative inaccuracy is ±0.5% in the extracted data of the MTL. The LAC of the fabricated ceramics was proven using the extracted data for MTL [28]:

$$LAC\ (cm^{-1}) = \frac{1}{x}\ln\left(\frac{I_o}{I_t}\right) \quad (1)$$

The thickness required to attenuate fifty percent of the incident photons was established and defines the half-value thickness (HVL, cm). Based on the LACs for the fabricated perovskite oxide ceramics, the HVL is expressed via Eq. (2). The thickness of the fabricated perovskite oxide ceramics exhibiting equivalent shielding efficacy to 0.05 cm of pure Pb, which was employed within lead rubber jackets at hospitals for the protection of patients and workers from the hazards of ionizing radiation, is referred to as the thickness equivalent to lead (TEL, cm). It can be determined based on the linear attenuation coefficients (LACs) of the prepared perovskite oxide ceramics and high-density materials such as pure Pb, as presented in Eq. (3) [29].

$$HVL\ (cm) = \frac{\ln(2)}{LAC} \quad (2)$$

$$TEL(cm) = \frac{X_{lead}\ln\left(\frac{I_o}{I_t}\right)_{ceramics}}{\ln\left(\frac{I_o}{I_t}\right)_{Pb}} \quad (3)$$

The ratio of γ-photons that are absorbed ($I_a$) photons by the prepared composites to the total number of incident photons ($I_o$) is known as the radiation protection efficiency (RPE, %). Eq. (4) shows how the RPE of the investigated ceramics was calculated [29].

$$RPE\ (\%) = \frac{I_a}{I_o} \times 100 \quad (4)$$

In addition to this, a second approach was employed to verify the simulated linear attenuation coefficient for the synthesis composites. The mass attenuation coefficient (MAC, $cm^2/g$) of the synthesis perovskite oxide ceramics is calculated by using the XCOM theoretical database. The MACs are then translated to the linear attenuation coefficients (LACs) using the following equation: MAC = LAC/ρ. The XCOM retrieves the sigma values, which are necessary for the computations of the shielding parameters, from the National Institute of Standards and Technology (NIST) database.

## 3. Results and discussion

### 3.1. XRD analysis

The prepared perovskite oxide ceramics' XRD patterns are presented in Fig. 1. These include BTO, STO, BNT, BKT, and BLT. In all of the samples, the typical diffraction peaks of a perovskite structure were observed. The BTO XRD pattern is a high match to the standard pattern JCPDS card No. 05–0626. The high intensity peak at around 45° 2θ confirms the formation of a pure tetragonal phase. The XRD pattern STO, on the other hand, the (110) reflection at about 32.3 2θ confirms formation of a cubic perovskite lattice with space group Pm3m, matching the standard STO pattern JCPDS No. 35–0734. The BNT ceramic exhibits an XRD pattern that matches the reference ICDD PDF

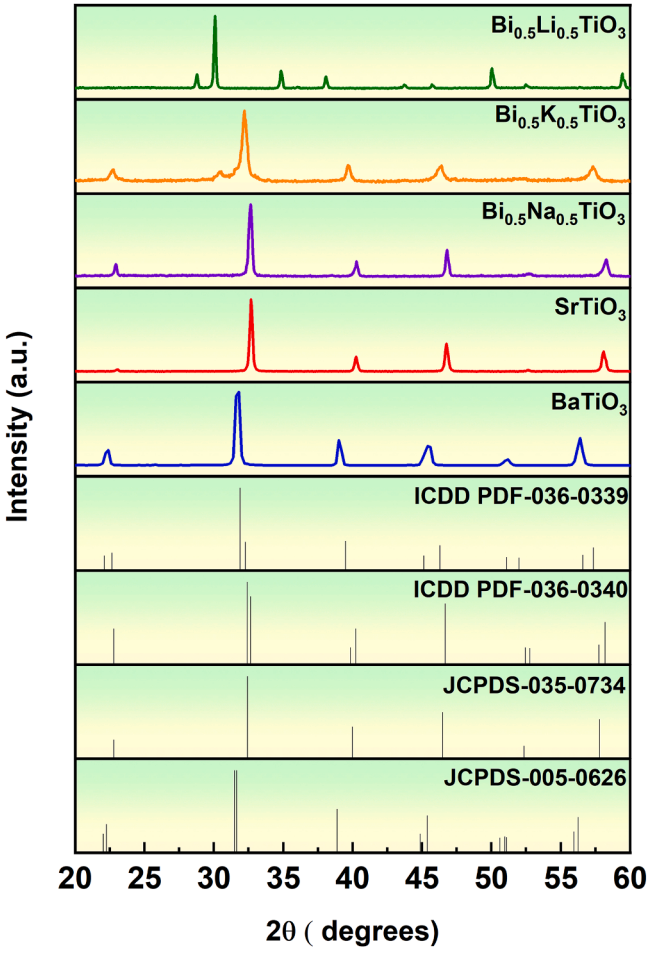


**Fig. 1.** Shows the crystal structure of BTO, STO, BNT, BKT, and BLT ceramics.

No. 36–0340 [21,30]. The rhombohedral phase is confirmed by the peak around 40° 2θ reflection (003)/(021) together with a peak about 46.5° 2θ reflection (202). Similarly, BKT is confirmed to form a perovskite phase; its reflections coincide with the standard pattern ICDD PDF No. 36–0339. The two peaks of the (002) and (200) planes are at around 44.4 and 46.5 2θ, indicating tetragonal symmetry in this material [16, 31]. The XRD pattern of BLT also shows the successful formation of a tetragonal structure and the XRD pattern matches the ICDD ref. No. 980, 064,716 [32]. In all samples prepared, no additional peaks were found, confirming the formation of perovskite single phase polycrystalline without any evidence of the existence or impurity of second phases. The formation of these solid crystalline structures is beneficial for radiation shielding applications because their dense lattices, which often contain heavy elements like Bi, that can block harmful radiation effectively.

Further quantitative analysis by Rietveld refinement approach was conducted to confirm the phase structures of the prepared perovskite oxides. This method fits the full diffraction profiles and provides refined lattice parameters and unit cell volume. Table 1 summarizes the refined structures results of BTO, STO, BNT, BKT, and BLT ceramics. BTO is tetragonal with space group P4mm (a = b = 3.994 Å, c = 4.038 Å, V = 64.414 Å$^3$) and STO is cubic space group Pm-3 m (a = b = c = 3.905 Å, V = 59.55 Å$^3$). The BNT ceramic fits a rhombohedral structure (a = b = 5.476 Å, c = 6.778 Å, V = 176.02 Å$^3$), while BKT is tetragonal phase (a = b = 3.918 Å, c = 4.013 Å, V = 61.60 Å$^3$), and BLT is cubic Pm-3 m (a = b = c = 5.152 Å, V = 136.8 Å$^3$). No secondary phases were required to obtain adequate fits, supporting phase purity within XRD limits.

### 3.2. Microstructure analysis

The five synthesized ceramics' SEM micrographs are shown in Fig. 2. The overall view clearly indicates that all ceramics show fine and uniform morphologies with shapes that are more likely to be spherical. The BTO ceramic exhibits a smaller particle with an approximate 95 nm average particle size, as shown in Fig. 2(a). Fig. 2 (b-e) shows a gradual increase in the average particle distribution of 200, 210, 144, and 780 nm, respectively, for the STO, BNT, BKT, and BLT ceramics. It should be noted that despite the same synthesis method being used for all ceramics. We observed a range of particle sizes between 95 and 780 nm. This is probably attributed to the fact that each composition has chemistry that controls grain boundary mobility and grain growth. The particle size and morphology can affect performance mainly by determining how the prepared ceramics become dense and uniform. The finer powders with uniform texture such as BTO at about 95 nm and BKT at about 144 nm are expected to have better packing and faster densification, which helps minimize large residual pores. This matters in shielding because pores reduce the effective density, and attenuation depends on mass thickness; a more porous ceramic will need more thickness to reach the same protection level. This trend is consistent with perovskite ceramics reported in the literature where increased densification leads to higher linear attenuation [33].

### 3.3. SCS analysis

Fig. 3 demonstrates a comparison of the SCSs of proton moving in $SrTiO_3$, $BaTiO_3$, $Bi_{0.5}Li_{0.5}TiO_3$, $Bi_{0.5}Na_{0.5}TiO_3$ and $Bi_{0.5}K_{0.5}TiO_3$ against experimental data for $SrTiO_3$ reported by Dedyulin et al. [34] along with projected proton ranges for five perovskite lead free ceramics. The electronic stopping data of the $ABO_3$ oxide perovskite family are deducted from SRIM code predictions via Bragg's rule of additivity [35, 36].

Fig. 3a shows all five ceramics to demonstrate the usual proton Bragg peak like maximum between 100 and 200 keV. The differences are below 30%, which is predictable owing to all being perovskite $ABO_3$ and oxygen predominating the stoichiometry. The variation in stopping data among these perovskites is governed by chemical bonding between two atoms [37], band-structure (e.g., density of states closer to the Fermi level and energy gap of ceramic), plasmon relaxation time [38], effective mean excitation energy I (eV), average Z/A per formula unit of perovskite, induced electron density, and the valence-electron response [39]. Table 2 presents the calculations of the average Z/A and molar mass for five perovskite ceramics, providing further insight into the variability in energy loss resulting from proton-perovskite interactions. The energy loss per atom of the $ABO_3$ perovskites exhibits the following SCS order: SCS ($BaTiO_3$) > SCS ($SrTiO_3$) > SCS ($Bi_{0.5}K_{0.5}TiO_3$) > SCS ($Bi_{0.5}Na_{0.5}TiO_3$) > SCS ($Bi_{0.5}Li_{0.5}TiO_3$). Within the Bismuth alkali group, when the Z/A value increases (i.e., (Z/A) $Bi_{0.5}K_{0.5}TiO_3$ > (Z/A) $Bi_{0.5}Na_{0.5}TiO_3$ > (Z/A) $Bi_{0.5}Li_{0.5}TiO_3$), the SCS values exhibit a corresponding trend. The calculation shows that $SrTiO_3$ has a relatively higher Z/A value compared to bismuth alkali compounds, which increases its proton energy loss relative to the ceramic perovskites involving bismuth at the energy loss peak. In contrast, $SrTiO_3$ stopping power results show that the differences between SRIM predictions obtained by Bragg's rule and experimental data [34] have the range deviations up to 25%, which leads to overestimation in theoretical results relative to experiment as reported by W. J. Weber et al. and M. Titze et al. [40,41]. Although $(Z/A)_{STO}$ >$(Z/A)_{BTO}$, the $BaTiO_3$ stopping results tend to have a larger SCS near the Bragg peak maximum than $SrTiO_3$ because it has a larger molar mass, and SCS is directly proportional to molar mass as emphasized in previous studies [42,43].

For the $ABO_3$ oxide perovskite family, the ceramic atomic number, chemical composition and density collectively influence the range and stopping power of charged particles in ceramic compounds. Based on the Bethe-Bloch stopping formula [44], the electronic stopping is proportional to the ceramic (Z/A) ratio and oscillator strength of the perovskite ceramic. In terms of radiation shielding efficiency, the proton's projected range is derived from stopping-power theory [45], depending primarily on the total atomic number per ceramic formula, $Z_{tot}$, and the ceramic's density. The values of the $Z_{tot}$ were 84, 89, 93, 97, and 102 for $SrTiO_3$, $Bi_{0.5}Li_{0.5}TiO_3$, $Bi_{0.5}Na_{0.5}TiO_3$, $Bi_{0.5}K_{0.5}TiO_3$ and $BaTiO_3$, respectively. Therefore, higher $Z_{tot}$ typically increases the proton's probability of slowing down and reduces the projected range in the $ABO_3$ perovskite compound. The proton projected ranges for five fabricated lead free ceramics are presented in Fig. 3b for proton kinetic energy up to T = 100 MeV. Projected range is a quantity that denotes the average values for the slowdown in the depth of ion penetration in matter. The proton range data followed the order: PR ($SrTiO_3$)> PR ($BaTiO_3$)> PR ($Bi_{0.5}Li_{0.5}TiO_3$)> PR ($Bi_{0.5}Na_{0.5}TiO_3$)> PR ($Bi_{0.5}K_{0.5}TiO_3$). Obviously, the proton projected range results tend to decline with swapping strontium with Barium or Bismuth alkali mixes, because the proton projected range has an inverse proportionality to the perovskite sample's density

**Table 1**
Rietveld refinement results for the prepared BTO, STO, BNT, BKT, and BLT perovskite oxides including the refined symmetry and space group, lattice parameters a, b, c, and unit cell volume (V).

| Code sample | Crystal system | Space group | Space group number | a (Å) | b (Å) | C (Å) | V (Å)$^3$ |
|---|---|---|---|---|---|---|---|
| $BaTiO_3$ sample | Tetragonal | P4mm | 99 | 3.994 | 3.994 | 4.038 | 64.414 |
| $SrTiO_3$ sample | Cubic | Pm-3m | 221 | 3.905 | 3.905 | 3.905 | 59.55 |
| $Bi_{0.50}Na_{0.50}O_3Ti$ | Rhombohedral | R | | 5.476 | 5.476 | 6.778 | 176.02 |
| $Bi_{0.5}K_{0.5}O_3Ti$ | Tetragonal | | | 3.918 | 3.918 | 4.013 | 61.60 |
| $Bi_{0.5}Li_{0.5}O_3Ti$ | Cubic | Pm-3m | 221 | 5.152 | 5.152 | 5.152 | 136.8 |

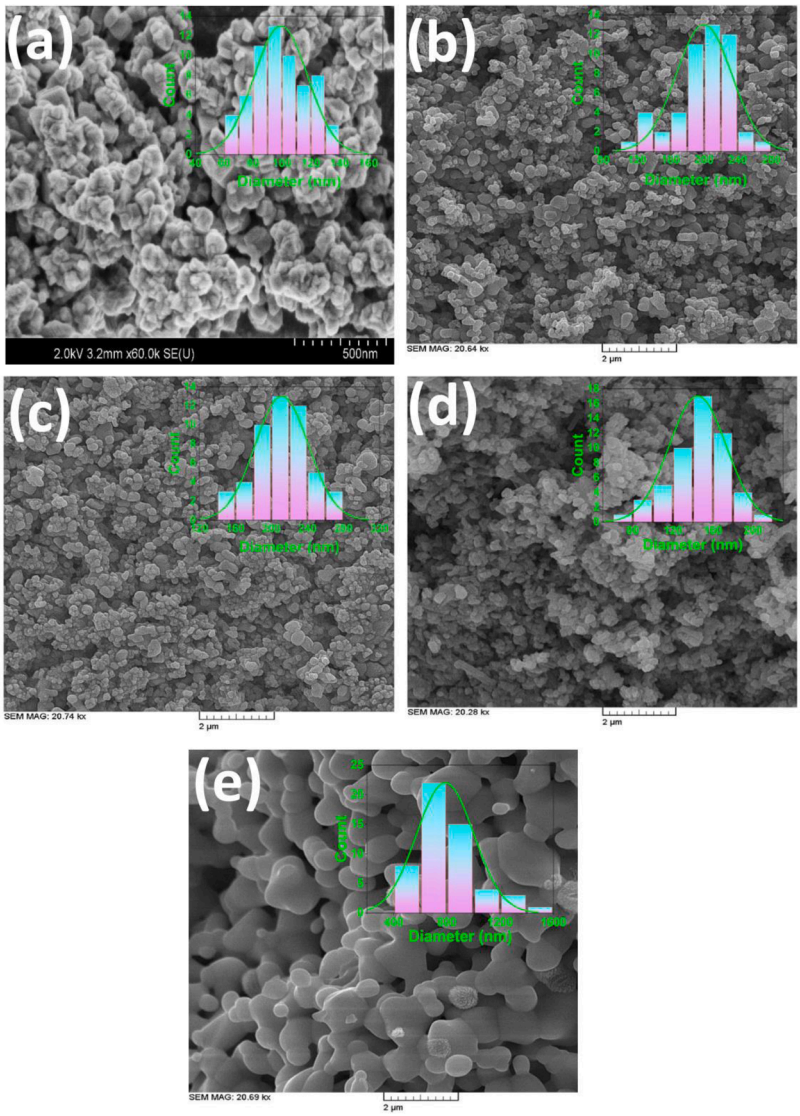


**Fig. 2.** The microstructure of (a) BTO, (b) STO, (c) BNT, (d) BKT, and (e) BLT ceramics.

over all T (MeV). The projected range at maximum kinetic energy T 100MeV varied from 21.49, 19.92, 19.61, 17.7and 17.24 mm for $SrTiO_3$, $BaTiO_3$, $Bi_{0.5}Li_{0.5}TiO_3$, $Bi_{0.5}Na_{0.5}TiO_3$ and $Bi_{0.5}K_{0.5}TiO_3$ respectively. Therefore, it can be inferred that $Bi_{0.5}K_{0.5}TiO_3$ is the best candidate for proton-shielding because $Bi_{0.5}K_{0.5}TiO_3$ has the lowest proton range of about 17.24 mm compared to other samples at T = 100MeV.

### 3.4. Gamma-ray shielding

The shielding parameters (SPs) are investigated for the synthesized composites along the 0.015–15 MeV γ-ray energy ($E_\gamma$) range, which are affected by the $E_\gamma$, doping compounds, and the sized composite thickness.

The effect of $E_\gamma$ appears due to the proportionality of the γ-ray interaction cross-section (σ) with $E_\gamma^{-3.5}$ (across the photoelectric interaction (PEI) interval), $E_\gamma^{-1}$ (across the Compton scattering interaction (CSI) interval), and Log $E_\gamma$ (across the pair production interaction (PPI) interval. As a result of these illustrated proportionalities of σ with $E_\gamma$, the σ values strongly reduced at the PEI region, followed by a moderate CSI region reduction, and suffered insignificant variation at the PPI region. This illustrated σ value reduction causes a decrease in the γ-photons/electrons interactions inside the synthase composites, leading to increased transmitted photons ($I_t$). This $I_t$ photon increase decreases the ($I_o/I_t$) ratio and the synthesized composites' LACs as the $E_\gamma$ increases, as Fig. 4 (a-c) illustrates. As the $E_\gamma$ increased along with the PE region in the 0.015–0.122 MeV range, the LACs strongly decline from 100.432 to 1.758 $cm^{-1}$ (for STO), 271.628 to 5.033 $cm^{-1}$ (for BTO), 426.658 to 11.751 $cm^{-1}$ (for BLT), 452.940 to 12.214 $cm^{-1}$ (for BNT), and 459.116 to 12.252 $cm^{-1}$ (for BKT), as Fig. 4a illustrates. This strong LAC reduction confirms the predominance of the PEI across the mentioned region. Following that, the CSI becomes more strongly associated with a diminution in the PE interaction. This increased CSI moderately declines the LACs of the synthesized composites, as Fig. 4b illustrates. The STO, BTO, BLT, BNT, and BKT's LACs decline from 1.758 to 0.297 $cm^{-1}$, 5.033 to 0.347 $cm^{-1}$, 11.751 to 0.400 $cm^{-1}$, 12.214 to 0.440 $cm^{-1}$, and 12.252 to 0.448 $cm^{-1}$, respectively. The PP interaction starts inside the synthesized composites when $E_\gamma \geq 1.022$ MeV. Across the energy region, which varied from 1.022 MeV to 10 MeV, the PEI, CSI, and PPI occur within the synthesized composites, but the CSI interaction is the predominant one. This assumption was affirmed by the observed decline in the LACs along the energy interval, which had a 1.022–10 MeV variation, as presented in Fig. 4c. The LACs of STO, BTO, BLT, BNT, and BKT decreased from 0.297 to 0.147 $cm^{-1}$, 0.347 to 0.203 $cm^{-1}$, 0.400 to 0.233 $cm^{-1}$, 0.440 to 0.253 $cm^{-1}$, and 0.448 to 0.257 $cm^{-1}$, respectively. Following that, as the $E_\gamma$ raised greater than 10 MeV, the LACs suffered an insignificant

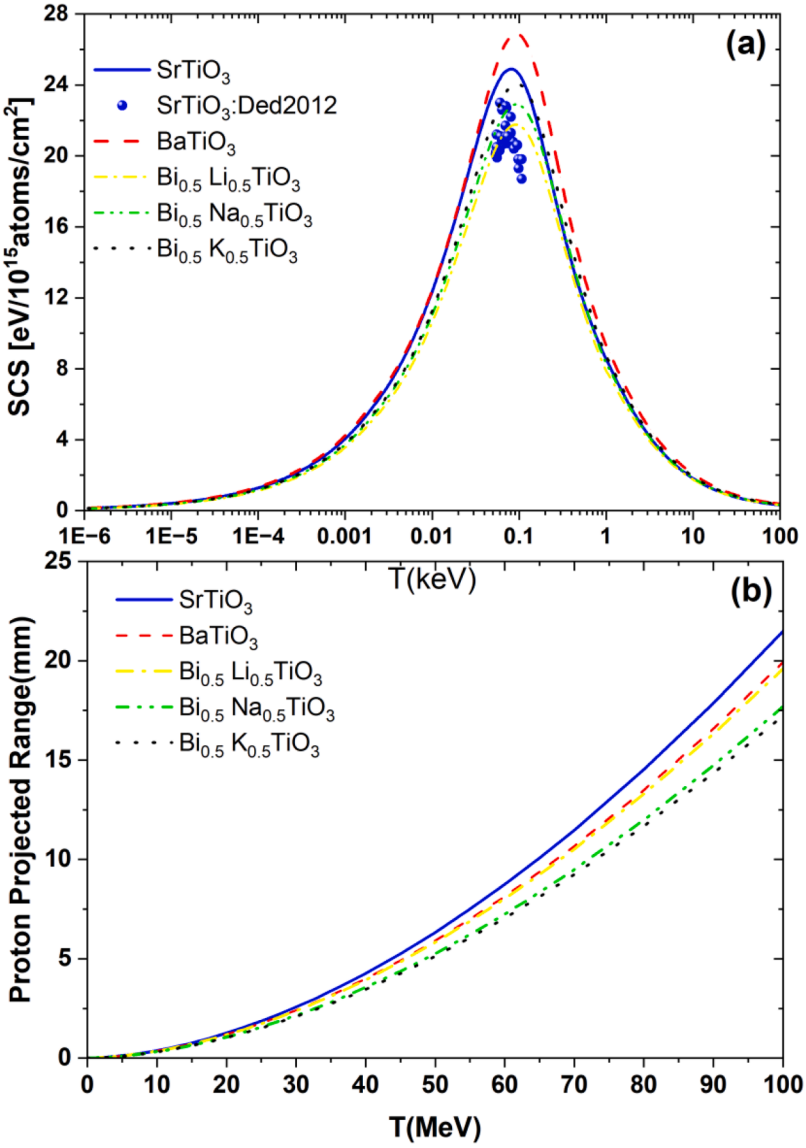


**Fig. 3.** (a) Electronic SCS as a function of broad proton kinetic energy range T (MeV) for $SrTiO_3$, $BaTiO_3$, $Bi_{0.5}Li_{0.5}TiO_3$, $Bi_{0.5}Na_{0.5}TiO_3$, and $Bi_{0.5}K_{0.5}TiO_3$ samples calculated using the SRIM program. The blue symbols indicate experimental results reported by Dedyulin et al. [34]., (b) Variations of PR versus proton energy range for different perovskite oxide ceramics.

**Table 2**
Perovskite lead free ceramics parameters calculated in this work.

| Sample | Formula | Molar Mass(g/mol) | Z/A |
|---|---|---|---|
| STO | $SrTiO_3$ | 183 | 0.458 |
| BTO | $BaTiO_3$ | 233 | 0.437 |
| BLT | $Bi_{0.5}Li_{0.5}TiO_3$ | 204 | 0.437 |
| BNT | $Bi_{0.5}Na_{0.5}TiO_3$ | 212 | 0.439 |
| BKT | $Bi_{0.5}K_{0.5}TiO_3$ | 220 | 0.441 |

increase as a result of the predominance of PPI.

Table 3 reveals agreement between the simulated LACs employing the MCNP-5 code and the calculations according to the XCOM database for the synthesized composites STO, BTO, BLT, BNT, and BKT. The calculated difference between both methodologies ranges ±2.5%. The difference between both methods was attributed to many factors. The first is the different nuclear libraries that support the programs with the interaction cross-sections for the elements constituting the fabricated samples. The XCOM program depends on the NIST nuclear library, while the MCNP-5 code depends on the ENDF/B.VI.8 nuclear library. Secondly, the XCOM calculation didn't consider the density and position of the examined samples from the radioactive source and the detector, while the MCNP-5 code did.

The MACs of the synthesized composites are determined according to the simulated LACs across the selected energy region, as seen in Fig. 4d Under the PEI, CSI, and PPI interactions' influence, the MACs of STO, BTO, BLT, BNT, and BKT diminish from 19.654 to 0.030 $cm^2/g$, 45.106 to 0.036 $cm^2/g$, 68.265 to 0.040 $cm^2/g$, 65.930 to 0.040 $cm^2/g$, and 65.494 to 0.040 $cm^2/g$, respectively.

The HVLs for the synthesized composites were calculated, where it has an increasing trend as the γ-ray energy increased, as Fig. 5 presents. The rising trend occurs owing to the σ decrease as the $E_\gamma$ increased, which causes a transmitted ($I_t$) photon increase. Hence, there is a fabricated composite thickness increase that is able to minimize the $I_t$ photons to 50% of $I_o$. Through the Fig. 5-presented data, the 0.015 to 10 MeV $E_\gamma$ enrichment is followed by the HVL growth of STO, BTO, BLT, BNT, and BKT from 0.007 to 4.705 cm, 0.003 to 3.421 cm, 0.002 to 2.975 cm, 0.002 to 2.741 cm, and 0.002 to 2.693 cm, respectively. After that, at a higher $E_\gamma$ than 10 MeV, a slight HVL decrease was observed for all synthesized composites. The slight decrease in the HVLs above 10

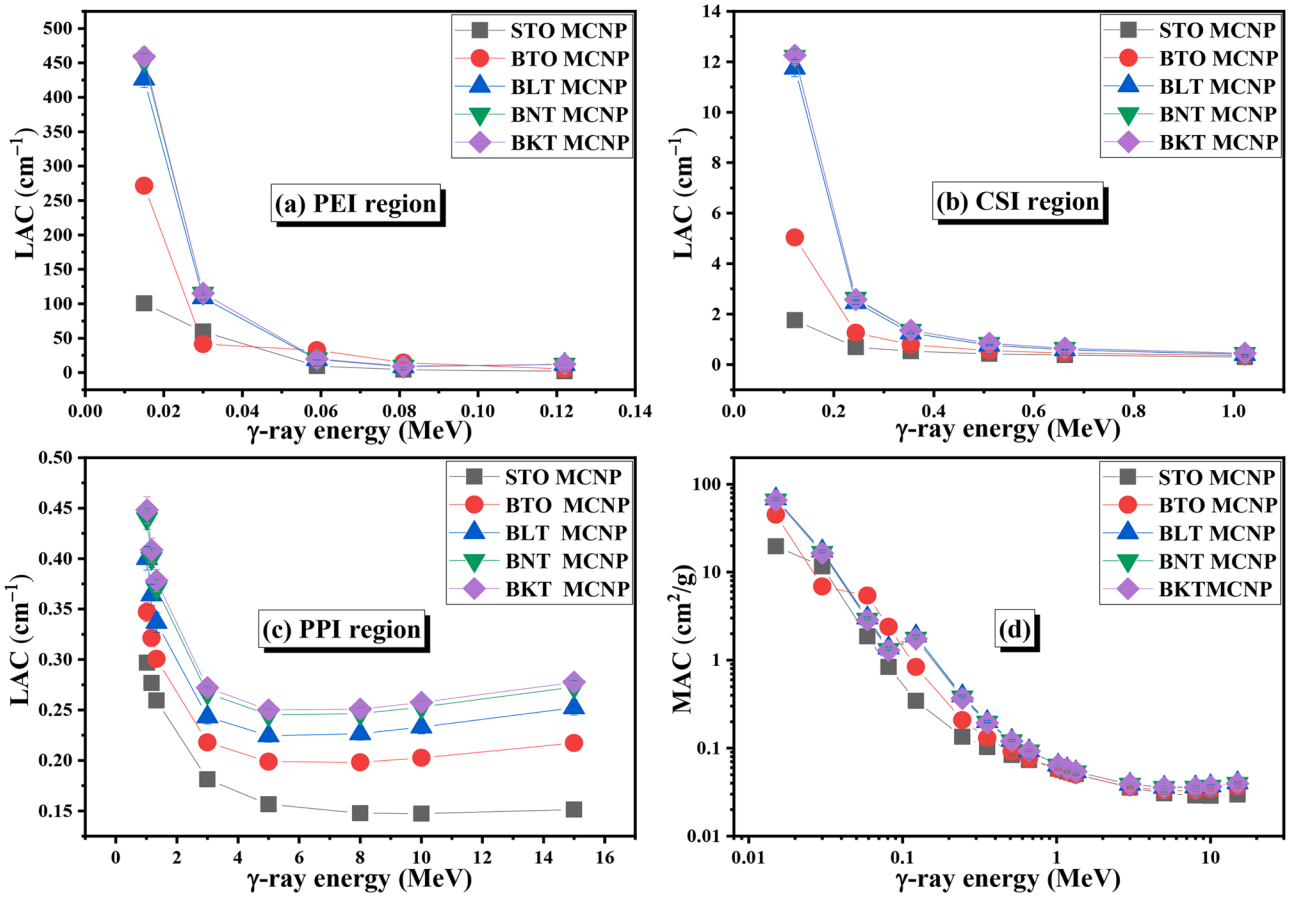


**Fig. 4.** The γ-ray energy's influence on (a) LAC at PEI region, (b) LAC at CSI region, (c) LAC at PPI region, and (d) total MACs of the synthesized composites.

MeV is attributed to the predominance of the PPI at E ≥ 10 MeV. The predominance of the PPI leads to a slight increase in the interaction cross section (σ), which results in a slight reduction in the transmitted ($I_t$) photons. Therefore, the $I_o/I_t$ ratio and LACs of the investigated glasses slightly increased, leading to a slight reduction in their HVL.

The $TE_L$ values were calculated for the synthesized shield composites based on the LACs of lead and synthesized shield composites [46,47]. At the PE interaction range, there are sharp increases in the $TE_L$s for composites of STO and BTO at energies of 0.03 and 0.122 MeV. These sharp increases are a result of the L1 and K absorption edges of lead, which cause increases in the LACs of pure lead compared to the synthesized composites (STO and BTO), which are rich with Sr and Ba, respectively. There aren't any observed peaks for composites BLT, BNT, and BKT due to their high content of Bi, which has L1 and K-absorption edges semi-equal to those of lead. According to the data presented in Fig. 6, the highest $TE_L$s observed for the synthesized composites STO, BTO, BLT, BNT, and BKT are at 0.122 MeV and reach 1.082 cm, 0.378 cm, 0.162 cm, 0.156 cm, and 0.155 cm, respectively. Additionally, Fig. 6 shows that, as $E_\gamma$ rose from 0.015 MeV to 0.244 MeV, the $TE_L$ fluctuated between 0.628 and 0.516 cm for STO, 0.232 and 0.283 cm for BTO, 0.148 and 0.145 for BLT, 0.139 and 0.136 cm for BNT, and 0.137 and 0.138 cm for BKT. Subsequently, the increment in the $E_\gamma$ values from 0.244 to 1.022 MeV results in a moderate diminishment in the $TE_L$s of the STO, BTO, BLT, BNT, and BKT from 0.516 to 0.132 cm, 0.283 to 0.113 cm, 0.145 to 0.098 cm, 0.136 to 0.089 cm, and 0.138 to 0.088 cm, respectively. This moderate reduction in the $TE_L$s is a result of the moderate reduction in the LACs of lead and synthesized composites, where the LACs of lead, STO, BTO, BLT, BNT, and BKT declined by 88.95%, 56.92%, 72.37%, 83.72%, 83.24%, and 82.60%, respectively. The raise in $E_\gamma$ quantities from 1.022 MeV to 3 MeV is consorted by a drooping in the $TE_L$s of synthesized composites. This reduction is quit smaller for STO and BTO composites than the reduction observed for the BLT, BNT, and BKT composites. This behavior is attributed to the decrease in the LACs of lead, which is higher than the decrease in the LACs of synthesized composites as the $E_\gamma$ increased across the PP interaction region from 1.022 MeV to 3 MeV. Thereafter, the boost in $E_\gamma$ from 3 MeV to 15 MeV causes an increase in the LACs of lead, STO, BTO, BLT, BNT, and BKT by 33.63%, −16.47%, −0.25%, 3.77%, 2.36%, and 2.01%. The significant increase in the LAC of lead, in contrast to the minimal increase in the LACs of synthesized composites, results in a rise in the $TE_L$s of fabricated composites as $E_\gamma$ increases from 3 to 15 MeV.

The $RP_E$ was calculated for the synthesized composites across the selected γ-ray energy range between 0.015 and 15 MeV, as presented in Fig. 7. The maximum values for the $RP_E$s were observed at the PE interaction region between 0.015 and 0.122 MeV. The $RP_E$s for the synthesized composites with a 1 cm thickness are close to 100% due to their high ability to absorb low-energy γ-ray photons during the PE interaction. Thereafter, as the $E_\gamma$ rises from 0.122 to 1.022 MeV across the CSI interaction region, the $RP_E$s reduce moderately. The $RP_E$s for the 1 cm thickness of synthesized composites STO, BTO, BLT, BNT, and BKT decline from 82.76 to 25.69%, 99.35 to 29.32%, 100.00 to 32.98%, 100.00 to 35.56%, and 100.00 to 36.12%. The mentioned moderate decline in the $RP_E$s is linked to the CSI interaction, where the σ values decrease moderately as the $E_\gamma$ rises, which leads to an increase in the ($I_t$) photons. Therefore, the absorbed ($I_a$) photons, ($I_a/I_o$), and $RP_E$s all declined as the $E_\gamma$ rose. Across the $E_\gamma$ region from 1.022 MeV to 10 MeV, the $RP_E$s are still decreasing as the $E_\gamma$ increases. At $E_\gamma \geq 10$ MeV, the $RP_E$s for all composites reduced with raising the $E_\gamma$ energy due to the increase of σ values and ($I_a$) photons with increasing $E_\gamma$ at high energies.

For further enhancement of the $RP_E$s of the synthesized composites, their thickness should be increased. The growth of composites' thickness increases the path length of γ-photons inside the composites, which

**Table 3**
The difference between the LACs simulated using the MCNP-5 code and those calculated using the XCOM program.

| Energy (MeV) | Linear attenuation coefficient (LAC, $cm^{-1}$) | | | | | | | | |
|---|---|---|---|---|---|---|---|---|---|
| | STO | | | BTO | | | BLT | | |
| | MCNP | XCOM | Diff (%) | MCNP | XCOM | Diff (%) | MCNP | XCOM | Diff (%) |
| 0.015 | 100.432 | 101.025 | 0.59 | 271.628 | 271.652 | 0.01 | 426.658 | 426.938 | 0.07 |
| 0.03 | 59.464 | 59.736 | 0.46 | 41.446 | 41.732 | 0.69 | 108.789 | 108.813 | 0.02 |
| 0.059 | 9.526 | 9.535 | 0.10 | 32.619 | 32.784 | 0.50 | 18.850 | 18.975 | 0.66 |
| 0.081 | 4.280 | 4.248 | −0.75 | 14.399 | 14.296 | −0.72 | 8.593 | 8.675 | 0.94 |
| 0.122 | 1.758 | 1.743 | −0.89 | 5.033 | 5.082 | 0.95 | 11.751 | 11.688 | −0.54 |
| 0.244 | 0.689 | 0.690 | 0.09 | 1.256 | 1.247 | −0.72 | 2.458 | 2.439 | −0.79 |
| 0.354 | 0.525 | 0.525 | 0.14 | 0.783 | 0.768 | −1.91 | 1.255 | 1.258 | 0.22 |
| 0.511 | 0.426 | 0.427 | 0.13 | 0.551 | 0.552 | 0.27 | 0.766 | 0.768 | 0.23 |
| 0.662 | 0.373 | 0.374 | 0.17 | 0.459 | 0.460 | 0.25 | 0.584 | 0.587 | 0.48 |
| 1.022 | 0.297 | 0.300 | 0.93 | 0.347 | 0.353 | 1.68 | 0.400 | 0.411 | 2.53 |
| 1.173 | 0.277 | 0.279 | 0.84 | 0.321 | 0.326 | 1.46 | 0.364 | 0.372 | 2.21 |
| 3 | 0.181 | 0.182 | 0.41 | 0.218 | 0.219 | 0.52 | 0.243 | 0.245 | 0.69 |
| 5 | 0.157 | 0.157 | 0.30 | 0.199 | 0.199 | 0.31 | 0.225 | 0.225 | 0.37 |
| 8 | 0.148 | 0.148 | 0.22 | 0.198 | 0.198 | 0.20 | 0.227 | 0.227 | 0.22 |
| 10 | 0.147 | 0.148 | 0.18 | 0.203 | 0.203 | 0.15 | 0.233 | 0.233 | 0.17 |
| 15 | 0.151 | 0.152 | 0.16 | 0.217 | 0.218 | 0.14 | 0.252 | 0.253 | 0.13 |

| Energy (MeV) | BNT | | | BKT | | |
|---|---|---|---|---|---|---|
| | MCNP | XCOM | Diff (%) | MCNP | XCOM | Diff (%) |
| 0.015 | 452.940 | 453.214 | 0.06 | 459.116 | 459.365 | 0.05 |
| 0.03 | 115.302 | 115.347 | 0.04 | 115.207 | 115.244 | 0.03 |
| 0.059 | 20.006 | 20.136 | 0.65 | 19.948 | 20.077 | 0.64 |
| 0.081 | 9.061 | 9.226 | 1.79 | 9.041 | 9.197 | 1.70 |
| 0.122 | 12.214 | 12.400 | 1.50 | 12.252 | 12.253 | 0.01 |
| 0.244 | 2.622 | 2.610 | −0.47 | 2.575 | 2.599 | 0.90 |
| 0.354 | 1.353 | 1.356 | 0.22 | 1.357 | 1.360 | 0.20 |
| 0.511 | 0.832 | 0.834 | 0.22 | 0.841 | 0.843 | 0.20 |
| 0.662 | 0.638 | 0.641 | 0.48 | 0.647 | 0.650 | 0.46 |
| 1.022 | 0.440 | 0.451 | 2.45 | 0.448 | 0.459 | 2.39 |
| 1.173 | 0.400 | 0.409 | 2.14 | 0.409 | 0.417 | 2.09 |
| 3 | 0.267 | 0.268 | 0.69 | 0.272 | 0.274 | 0.68 |
| 5 | 0.245 | 0.246 | 0.37 | 0.250 | 0.251 | 0.35 |
| 8 | 0.246 | 0.247 | 0.22 | 0.251 | 0.251 | 0.21 |
| 10 | 0.253 | 0.253 | 0.15 | 0.257 | 0.258 | 0.17 |
| 15 | 0.273 | 0.273 | 0.13 | 0.278 | 0.278 | 0.12 |

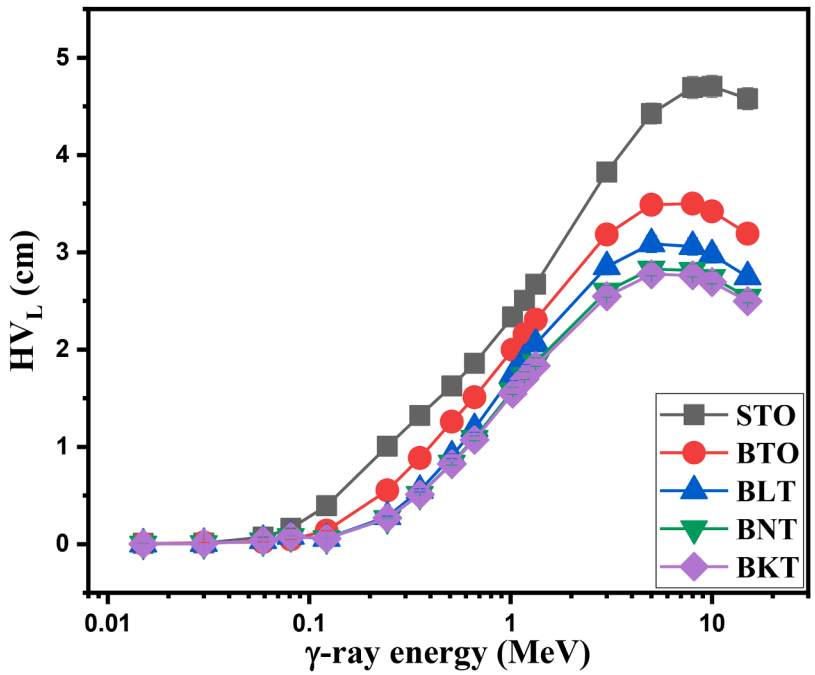


**Fig. 5.** The variation of half-value thickness ($HV_L$, cm) of synthesized composites as a function of γ-ray energy.

raises the probability of interaction of γ-photons with the composite's electrons [48]. Therefore, the ($I_a$) photons, ($I_a/I_o$), and the $RP_E$s of

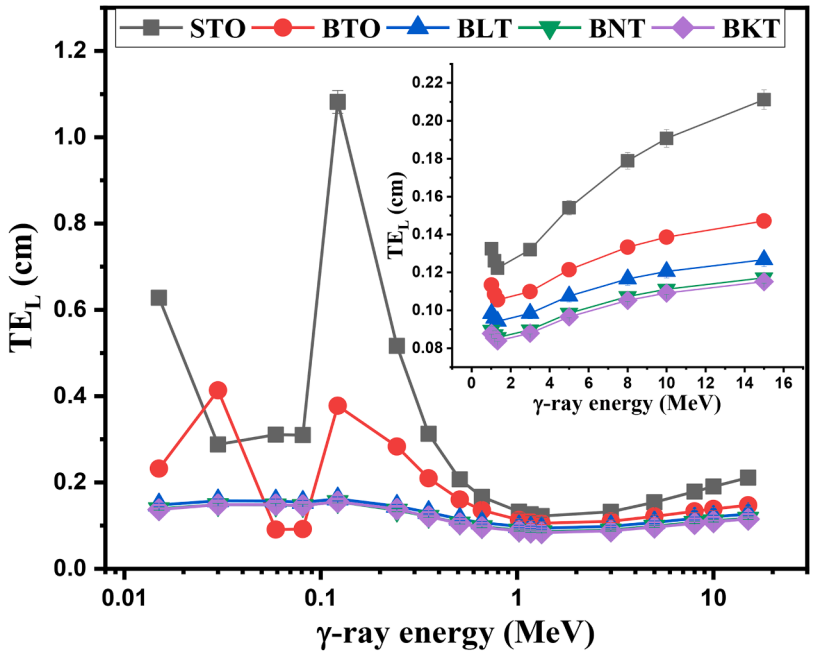


**Fig. 6.** The fluctuation of the thickness equivalent lead ($TE_L$, cm) with increasing the γ-ray energy.

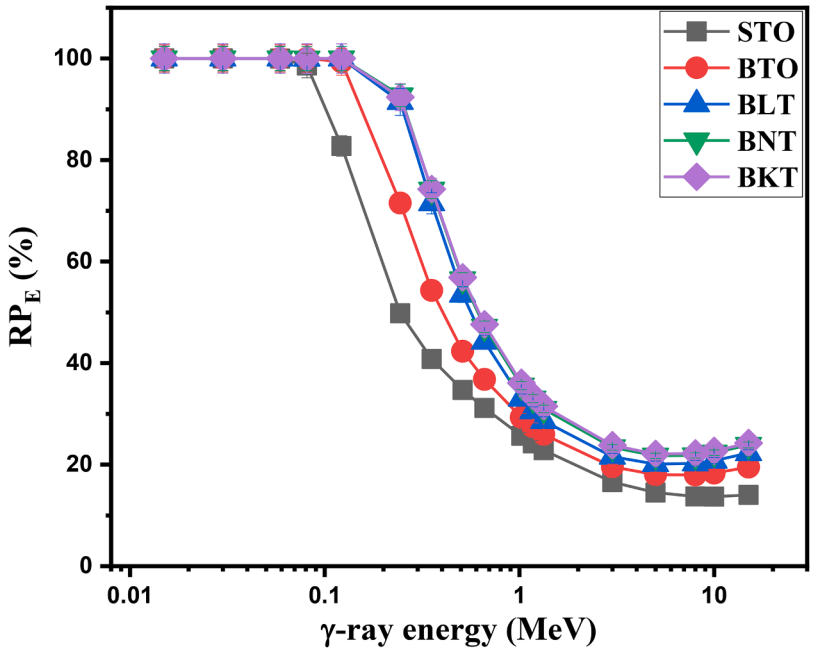


**Fig. 7.** The variation of the radiation protection efficiency ($RP_E$, %) of the synthesized composites versus the γ-ray energy.

synthesized composites rose with increasing the composite thickness. According to the data in Fig. 8, the growth of the composite's thickness from 0.25 to 2 cm enhances the $RP_E$s of STO, BTO, BLT, BNT, and BKT from 8.91 to 52.59%, 10.84 to 60.05%, 13.59 to 68.90%, 14.74 to 72.07%, and 14.93 to 72.58%, at energy of 0.662 MeV.

The type of dopant has a significant effect on the density (ρ, g/cm$^3$) of the synthesized composites, as presented in Fig. 9. The smallest ρ value is observed for the STO composite, which is rich in Sr (≈ 2.6 g/cm$^3$). Then changing the dopant changes the density of the synthesized composites. The ρ values for the fabricated composites have the order of BKT (7.01 g/cm$^3$) > BNT 6.87 g/cm$^3$) > BLT (6.25 g/cm$^3$) > BTO (6.02 g/cm$^3$) > STO (5.11 g/cm$^3$). The mentioned order is attributed to the ρ values for the utilized dopant, where the ρ value for $Bi_{0.5}K_{0.5}$ (5.33 g/cm$^3$) ≥ $Bi_{0.5}Na_{0.5}$ (5.38 g/cm$^3$) > $Bi_{0.5}Li_{0.5}$ (5.17 g/cm$^3$) > Ba (3.59 g/cm$^3$) > Sr (2.64 g/cm$^3$). Additionally, the increase in the ρ values of the synthesized composites may be attributed to their electron density and effective atomic number ($Z_{eff}$) of the synthesized composites. The effective atomic number ($Z_{eff}$) of the synthesized composites is ordered as follows: BKT (64.70) > BNT (65.48) > BLT (66.34) > BTO (47.14) > STO (30.67).

The effective atomic number ($Z_{eff}$) of the synthesized composites has a significant effect on their SPs due to the proportionality of σ values with $Z_{eff}^{4.6}$ (across the PEI region), $Z_{eff}$ (across the CSI region), and $Z_{eff}^{2}$ (across the PPI region) interaction regions. The increase in $Z_{eff}$ of fabricated composites increases σ values, which causes an increase in the

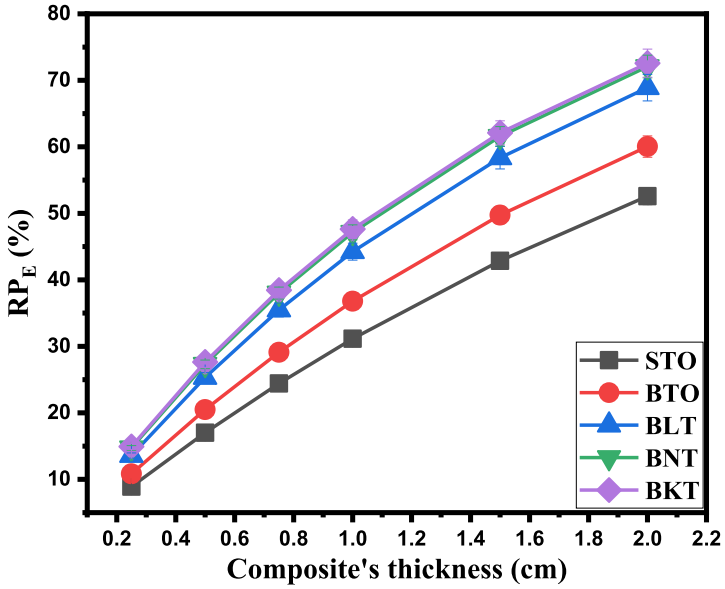


**Fig. 8.** Impact of the composites' thickness on their radiation protection efficiency ($RP_E$, %).

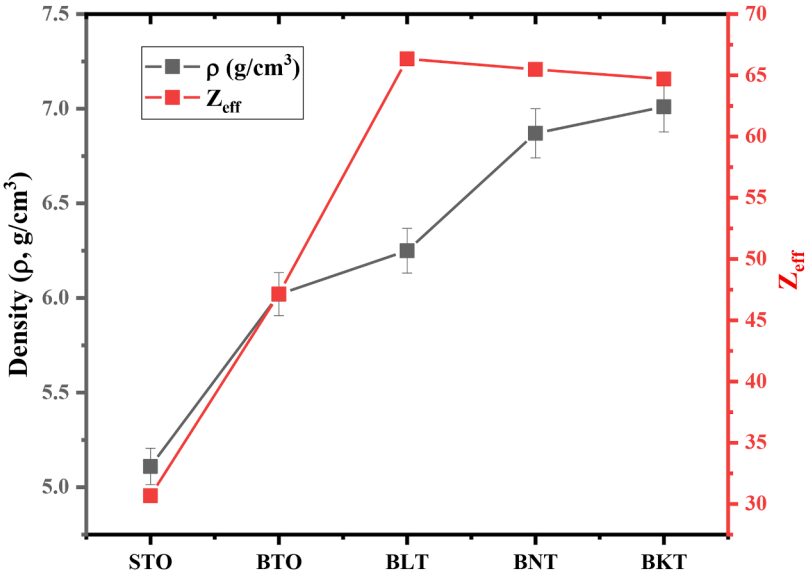


**Fig. 9.** The impact of various dopants on the density (ρ, g/cm$^3$) and effective atomic number ($Z_{eff}$) of the synthesized composites.

γ-photon/electron interactions within the synthesized composite layer [29,49,50]. Subsequently, the number of transmitted ($I_t$) photons decreased, resulting in an increase in the ($I_o/I_t$) ratio and LACs values, as illustrated in Fig. 10a. At 0.662 MeV, the LACs of the synthesized composites have the order of STO (0.373 cm$^{-1}$) < BTO (0.459 cm$^{-1}$) < BLT (0.584 cm$^{-1}$) < BNT (0.638 cm$^{-1}$) < BKT (0.647 cm$^{-1}$). The order of the LACs at 1.332 MeV is the same as illustrated previously, but it is slightly different at 0.059 MeV. At 0.059 MeV, the composite with dopant of Ba has the highest LAC due to the K-absorption edges of Ba, which appear at 0.0374 MeV and cause the LAC of the composite doped with Ba (i.e., BTO) to increase compared to other synthesized composites. Due to the reverse proportionality of the LACs and $HV_L$s for the synthesized composite, the composites with the highest LACs have the thinner $HV_L$s across all studied energies. Fig. 10b shows that the $HV_L$s of the synthesized composites at 0.662 MeV have the order of STO (1.857 cm) > BTO (1.511 cm) > BLT (1.187 cm) > BNT (1.087 cm) > BKT (1.071 cm).

The $TE_L$s for the synthesized composites have the same order as that presented for the $HV_L$s. The BKT composite has the thinnest $TE_L$s, measuring 0.096 cm at 0.662 MeV and 0.084 cm at 1.332 MeV, respectively (Fig. 10c). These lower $TE_L$s are attributed to the high density of the synthesized composite, which increases their LACs to be 52% and 60% of the LACs of pure lead at 0.662 MeV and 1.332 MeV, respectively. On the other hand, the highest $TE_L$s were observed for the STO composite, where its LACs at 0.662 and 1.332 MeV reach 30% and 40% of the LACs of pure lead.

Furthermore, the impact of dopant concentration on the $RP_E$s of the prepared composites was described in Fig. 10d At 0.059 MeV, the $RP_E$s for all composites are close to 100% due to the PE interaction's predominance. Therefore, all the dopants have the same effect on the $RP_E$s at 0.059 MeV. On the other hand, at 0.662 MeV and 1.332 MeV, the highest $RP_E$s were observed for the BKT composite with Bi0.5K0.5

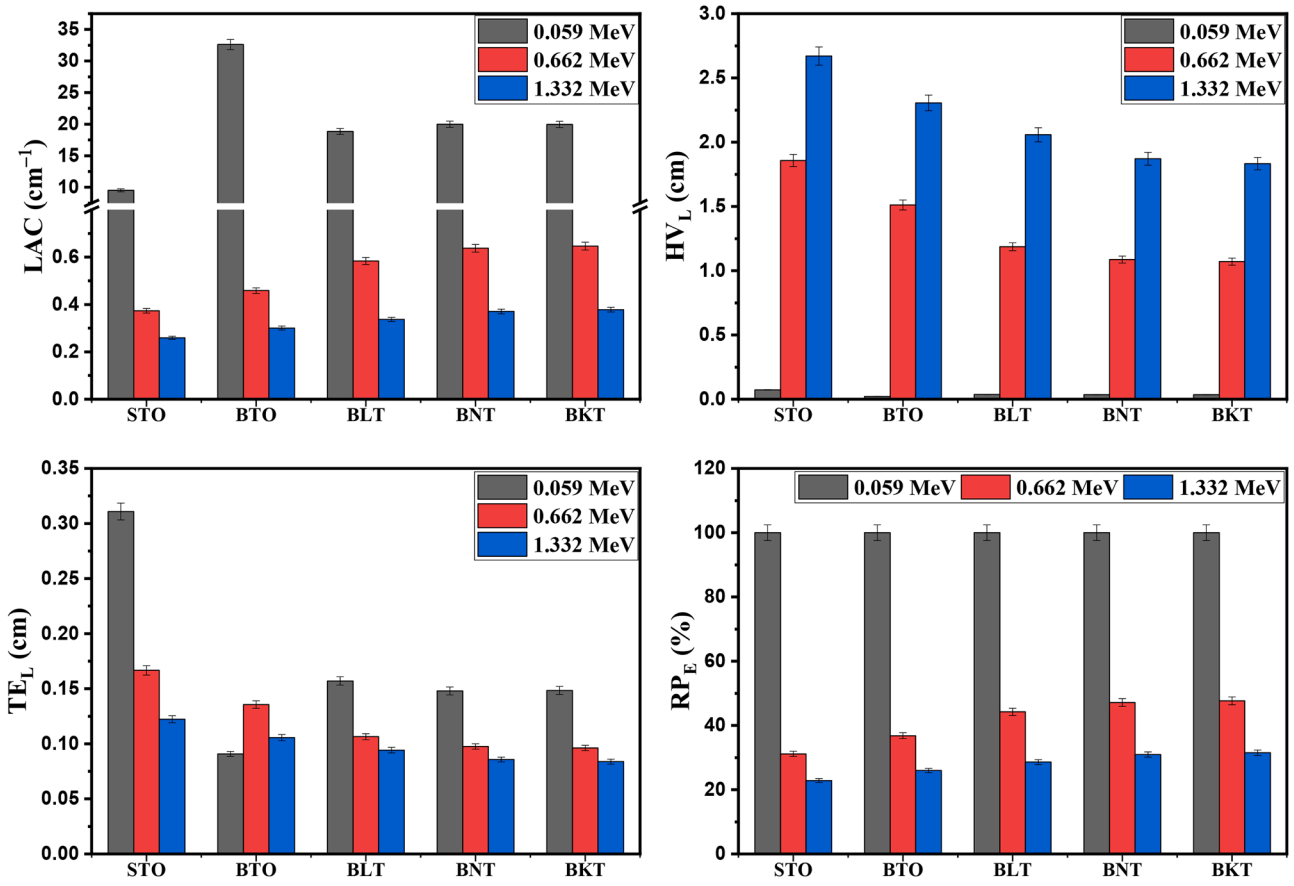


**Fig. 10.** The impact of various dopant on (a) LAC (cm$^{-1}$), (b) $HV_L$ (cm), (c) $TE_L$ (cm), and (d) $RP_E$ (%) of the synthesized composites.

dopant. These high $RP_E$s for BKT are attributed to its high σ values, which are responsible for increasing the ($I_a$) and ($I_a/I_o$) to reach high levels.

## 4. Conclusion

In summary, five different compositions of titanate-based perovskite oxide ceramics have been synthesized using the solid-state reaction method. All ceramics exhibited the expected crystalline phase corresponding to their titanate-based perovskite crystalline structures. The SEM results demonstrated the formation of uniform morphology for all compositions, mainly within a nanoscale size. The stopping and range results show that density, molar mass and average Z/A of perovskite ceramic can be related to the proton-absorbing shielding. At proton energy 100MeV, the lowest proton projected range is found to be about RP=17.24 mm for $Bi_{0.5}K_{0.5}TiO_3$ among Barium or Bismuth alkali mixes. The Monte Carlo simulation confirms that the substitution of Sr ions by Ba, ($Bi_{0.5}Li_{0.5}$), ($Bi_{0.5}Na_{0.5}$), and ($Bi_{0.5}K_{0.5}$) enhances the linear attenuation coefficient of the prepared composites. At 0.662 MeV, the linear attenuation coefficient for the prepared composites with chemical compositions of $SrTiO_3$, $BaTiO_3$, $Bi_{0.5}Li_{0.5}TiO_3$, $Bi_{0.5}Na_{0.5}TiO_3$, and $Bi_{0.5}K_{0.5}TiO_3$ reaches 0.373 cm$^{-1}$, 0.459 cm$^{-1}$, 0.584 cm$^{-1}$, 0.638 cm$^{-1}$, and 0.647 cm$^{-1}$, respectively. The optimal linear attenuation coefficient attained with the $Bi_{0.5}K_{0.5}TiO_3$ and $Bi_{0.5}Na_{0.5}TiO_3$ composites leads to their high radiation protection efficiency, where a thickness of 1 cm of the $Bi_{0.5}K_{0.5}TiO_3$ and $Bi_{0.5}Na_{0.5}TiO_3$ composites provides a radiation protection efficiency of around 48% at 0.662 MeV. The substitution of Sr ions with ($Bi_{0.5}K_{0.5}$) or ($Bi_{0.5}Na_{0.5}$) significantly boosts the shielding efficacy of the produced composites, yielding novel composites with adequate shielding performance for use as lead-free materials in radiation shielding applications.

## CRediT authorship contribution statement

**Rahman I. Mahdi:** Writing – review & editing, Writing – original draft, Methodology, Investigation. **K.A. Mahmoud:** Writing – review & editing, Writing – original draft, Methodology, Investigation. **Nabil Janan Al-Bahnam:** Writing – review & editing, Writing – original draft, Methodology, Investigation. **M.I. Sayyed:** Writing – review & editing, Writing – original draft, Methodology, Investigation. **Kawa M. Kaky:** Writing – review & editing, Writing – original draft, Methodology, Investigation. **Abed Jawad Kadhim:** Writing – review & editing, Writing – original draft, Methodology, Investigation. **Yasser Maghrbi:** Writing – review & editing, Writing – original draft, Methodology, Investigation.

## Declaration of competing interest

The authors declare that they have no known competing financial interests or personal relationships that could have appeared to influence the work reported in this paper.

## Data availability

Data will be made available on request.

## References

[1] J. Sobczak, G. Żyła, Nano and microcomposites as gamma and X-ray ionizing radiation shielding materials — A review, Energy 290 (2024) 130210.
[2] L. Yu, et al., Lightweight polyester fabric with elastomeric bismuth titanate composite for high-performing lead-free X-ray shielding, Radiat. Phys. Chem. 205 (2023) 110726.
[3] C.G. Hernandez-Murillo, et al., X-ray and gamma ray shielding behavior of concrete blocks, Nucl. Eng. Technol. 52 (8) (2020) 1792–1797.

[4] A.M. Onaizi, et al., Radiation-shielding concrete: a review of materials, performance, and the impact of radiation on concrete properties, J. Build. Eng. 97 (2024) 110800.
[5] J. Kaewkhao, A. Pokaipisit, P. Limsuwan, Study on borate glass system containing with Bi2O3 and BaO for gamma-rays shielding materials: comparison with PbO, J. Nucl. Mater. 399 (1) (2010) 38–40.
[6] K. Xi, et al., Thermally stable piezoelectric properties of lead-free ceramics featuring polar topological domains, Acta Mater. 294 (2025) 121152.
[7] M. Wu, et al., Significantly enhanced piezoelectric properties of BaTiO3-based ceramics with unchanged curie temperature via local chemical inhomogeneity, Chem. Eng. J. 518 (2025) 164844.
[8] R.I. Mahdi, et al., Nanostructured LNTO saturable absorber for generating multi-wavelength laser in Q-switched EDFL, Opt. Mater. 157 (2024) 116122.
[9] M.M. Najm, et al., Performance investigation and optimization of EDFL based on lithium niobate–Titanium oxide nanomaterial saturable absorber, Opt. Mater. 165 (2025) 117118.
[10] R. Mahdi, et al., High-performance (K,Na)NbO3-based binary lead-free piezoelectric ceramics modified with acceptor metal oxide, Ceram Int. 46 (13) (2020) 21762–21770.
[11] S.-S. Ryu, et al., Characterization of mechanical properties of $BaTiO_3$ceramic with different types of sintering aid by nanoindentation, J. Ceram. Soc. Jpn. 117 (1367) (2009) 811–814.
[12] H. Yamaguchi, J. Tatami, M. Iijima, Measurement of mechanical properties of $BaTiO_3$layer in multi-layered ceramic capacitor using a microcantilever beam specimen, J. Ceram. Soc. Jpn. 127 (6) (2019) 335–338.
[13] S. Selvi, K. Marimuthu, G. Muralidharan, Effect of PbO on the B2O3–TeO2–P2O5–BaO–CdO–Sm2O3 glasses - structural and optical investigations, J. Non Cryst. Solids 461 (2017) 35–46.
[14] G. Panomsuwan, O. Takai, N. Saito, Optical and mechanical properties of transparent SrTiO3 thin films deposited by ECR ion beam sputter deposition, Phys. Status Solidi (a) 210 (2) (2013) 311–319.
[15] D. Lin, K.W. Kwok, H.L.W. Chan, Structure and electrical properties of Bi0.5Na0.5TiO3–BaTiO3–Bi0.5Li0.5TiO3 lead-free piezoelectric ceramics, Solid State Ion. 178 (37) (2008) 1930–1937.
[16] R.I. Mahdi, et al., Optimization of sintering temperature for the enhancement of pyroelectric properties of lead-free 0.88(Na0.5Bi0.5)TiO3–0.084(K0.5Bi0.5)TiO3–0.036BaTiO3 piezoelectric ceramics, J. Alloys Compd. 688 (2016) 77–87.
[17] M.I. Morozov, et al., Lead-free relaxor-like 0.75Bi0.5K0.5TiO3 –0.25BiFeO3 ceramics with large electric field-induced strain, Ferroelectrics 439 (1) (2012) 88–94.
[18] M. Asgari, et al., Comparison of nano/micro lead, bismuth and tungsten on the gamma shielding properties of the flexible composites against photon in wide energy range (40 keV–662 keV), Nucl. Eng. Technol. 53 (12) (2021) 4142–4149.
[19] N.D. Quan, et al., Current development in lead-free Bi0.5(Na,K)0.5TiO3-based piezoelectric materials, Adv. Mater. Sci. Eng. 2014 (1) (2014) 365391.
[20] R.I. Mahdi, W.H.A. Majid, Piezoelectric and pyroelectric properties of BNT-base ternary lead-free ceramic-polymer nanocomposites under different poling conditions, RSC Adv. 6 (84) (2016) 81296–81309.
[21] R.I. Mahdi, et al., Ferroelectric polarization and pyroelectric activity of functionalized P(VDF-TrFE) thin film lead free nanocomposites, Polym 141 (2018) 184–193.
[22] R.B. Malidarre, I. Akkurt, Simulation of neutron and gamma radiation shielding properties of KNN-LMN lead-free relaxor ceramics, J. Aust. Ceram. Soc. 59 (1) (2023) 137–143.
[23] A.A. Bendary, et al., Effect of replacing B2O3 with Dy2O3 on the structural, physical, and radiation shielding properties of sodium boroaluminate glass, J. Aust. Ceram. Soc. 60 (2) (2024) 455–469.
[24] A. Acevedo-Del-Castillo, et al., A brief review on the high-energy electromagnetic radiation-shielding materials based on polymer nanocomposites, Int. J. Mol. Sci. 22 (2021), https://doi.org/10.3390/ijms22169079.
[25] X. Zhong, et al., Improved relaxor behavior and insulation in BaTiO3-based ceramics for high-performance energy storage via trace MnO2 doping, Ceram Int. 51 (30, Part C) (2025) 66103–66112.
[26] M. Tihtih, et al., Role of A-site (Sr), B-site (Y), and A, B sites (Sr, Y) substitution in lead-free BaTiO3 ceramic compounds: structural, optical, microstructure, mechanical, and thermal conductivity properties, Ceram. Int. 49 (2) (2023) 1947–1959.
[27] A.M.A. El-Soad, M.W. Marashdeh, K.A. Mahmoud, Sustainable radiation protection epoxy with calcined clay and recycled metallic waste additives: analysis of structural, thermal, and gamma-ray shielding, J. Radiat. Res. Appl. Sci. 18 (4) (2025) 102057.
[28] R.I. Mahdi, et al., Tuning radiation attenuation performance of W-substituted nano-$BiNb_{1-x}W_xO_4$ ceramics: a Monte Carlo simulation approach, Mater. Today Commun. 51 (2026) 114918.
[29] R.I. Mahdi, et al., Engineered composition and morphology: unveiling 2D $bi_2(W_{1-x}Mox)O_6$ nanosheets for enhanced optical and ionizing protection applications, Mater. Today Commun. 45 (2025) 112415.
[30] R.I. Mahdi, et al., Ferroelectric and pyroelectric properties of novel lead-free polyvinylidenefluoride-trifluoroethylene–Bi0.5Na0.5TiO3 nanocomposite thin films for sensing applications, Ceram Int. 41 (10, Part A) (2015) 13836–13843.
[31] I. Krad, et al., Preparation and characterization of K0.5Bi0.5TiO3 particles synthesized by a stirring hydrothermal method, Ceram Int. 42 (3) (2016) 3751–3756.
[32] M. Nayak, M.R. Panigrahi, Quantitative structural analysis, phase transition and relaxor nature of Bi0.5Li0.5TiO3 ceramic prepared by mechanical alloying, J. Mater. Sci.: Mater. Electron. 27 (8) (2016) 8312–8318.
[33] E. Hannachi, et al., Theoretical examination of the radiation protecting properties of CaTiO3 material sintered at different temperatures, Crystals 13 (2023) 120, https://doi.org/10.3390/cryst13010120.
[34] S.N. Dedyulin, et al., Energy loss of protons in SrTiO3 studied by medium energy ion scattering, Nucl. Instrum. Methods Phys. Res. B: Beam Interact. Mater. At. 288 (2012) 60–65.
[35] J.F. Ziegler, M.D. Ziegler, J.P. Biersack, SRIM – the stopping and range of ions in matter (2010), Nucl. Instrum. Methods Phys. Res. B: Beam Interact. Mater. At. 268 (11) (2010) 1818–1823.
[36] W.H. Bragg, R. Kleeman XXXIX, On the α particles of radium, and their loss of range in passing through various atoms and molecules, Lond. Edinb. Dublin Philos. Mag. J. Sci. 10 (57) (1905) 318–340.
[37] D.I. Thwaites, Departures from Bragg's rule of stopping power additivity for ions in dosimetric and related materials, Nucl. Instrum. Methods Phys. Res. B: Beam Interact. Mater. At. 69 (1) (1992) 53–63.
[38] N.J. Al-Bahnam, et al., Describing the differential inelastic inverse mean free path of PMMA polymer with the Mermin–Belkacem-Sigmund model, Indian J. Phys. 97 (9) (2023) 2599–2610.
[39] N.J. Al-Bahnam, R.I. Mahdi, A.I.A. Al-Numan, The induced electron density effects of swift heavy ions in polymethyl methacrylate, Braz. J. Phys. 49 (1) (2019) 1–9.
[40] W.J. Weber, Y. Zhang, Predicting damage production in monoatomic and multi-elemental targets using stopping and range of ions in matter code: challenges and recommendations, Curr. Opin. Solid State Mater. Sci. 23 (4) (2019) 100757.
[41] M. Titze, et al., Evaluation of the accuracy of stopping and range of ions in matter simulations through secondary ion mass spectrometry and Rutherford backscattering spectrometry for low energy heavy ion implantation, J. Vac. Sci. Technol. A 39 (6) (2021).
[42] P. de Vera, I. Abril, R. Garcia-Molina, Electronic cross section, stopping power and energy-loss straggling of metals for swift protons, alpha particles and electrons, Front. Mater. 10 (2023).
[43] F. Salvat, Bethe stopping-power formula and its corrections, Phys. Rev. A 106 (3) (2022) 032809.
[44] J.F. Ziegler, Stopping of energetic light ions in elemental matter, J. Appl. Phys. 85 (3) (1999) 1249–1272.
[45] E. Kavaz, et al., The mass stopping power /projected range and nuclear shielding behaviors of barium bismuth borate glasses and influence of cerium oxide, Ceram Int. 45 (12) (2019) 15348–15357.
[46] R.I. Mahdi, et al., Transparent heavy-metal glass-ceramics reinforced with nano-PbO for next-generation X- and γ-ray shielding applications, Mater. Res. Bull. 195 (2026) 113808.
[47] K.A. Mahmoud, et al., Investigating the physical parameters, optical properties, mechanical features, and ionizing shielding efficiency of germanate-tellurite-borate glass-doped praseodymium oxide, J. Mater. Eng. Perform (2025).
[48] R.I. Mahdi, et al., Role of nano-bismuth oxide in tailoring the structural, mechanical, and optical behaviour of boro-tellurite glasses with enhanced radiation absorption, Ceram Int. (2025).
[49] K.M. Kaky, et al., Comprehensive investigations of niobium pentoxide effects on B2O3–TeO2-GeO2-MgO glass system for optical and radiation absorption applications, Radiat. Phys. Chem. 232 (2025) 112612.
[50] M.H.A. Mhareb, et al., Tailoring the optical, mechanical, and gamma-ray-attenuation performance of G-T-B glasses by doping nano rare-earth (Gd, Yb, Tm), Radiat. Phys. Chem. 237 (2025) 113019.